Title

Collagen microarchitecture mechanically controls myofibroblast differentiation

Journal

Proceedings of the National Academy of Sciences of the United States of America, 117(21)

ISSN

0027-8424

Authors

Seo, Bo Ri
Chen, Xingyu
Ling, Lu
et al.

Publication Date

2020-05-26

DOI

10.1073/pnas.1919394117

Peer reviewed

Collagen microarchitecture mechanically controls myofibroblast differentiation

Bo Ri Seo[a,b], Xingyu Chen[c,d], Lu Ling[a], Young Hye Song[a], Adrian A. Shimpi[a], Siyoung Choi[a], Jacqueline Gonzalez[a], Jiranuwat Sapudom[e], Karin Wang[a,f], Roberto Carlos Andresen Eguiluz[f], Delphine Gourdon[f,g], Vivek B. Shenoy[c,d], and Claudia Fischbach[a,h,1]

[a]Nancy E. and Peter C. Meinig School of Biomedical Engineering, Cornell University, Ithaca, NY 14853; [b]John A. Paulson School of Engineering and Applied Sciences, Harvard University, Cambridge, MA 02138; [c]Center for Engineering Mechanobiology, University of Pennsylvania, Philadelphia, PA 19104; [d]Department of Materials Science and Engineering, University of Pennsylvania, Philadelphia, PA 19104; [e]Biophysical Chemistry, Faculty of Life Sciences, Leipzig University, 04103 Leipzig, Germany; [f]Department of Materials Science and Engineering, Cornell University, Ithaca, NY 14853; [g]Department of Physics, University of Ottawa, Ottawa, ON K1N 6N5, Canada; and [h]Kavli Institute at Cornell for Nanoscale Science, Cornell University, Ithaca, NY 14853

Edited by David A. Weitz, Harvard University, Cambridge, MA, and approved March 24, 2020 (received for review November 12, 2019)

Altered microarchitecture of collagen type I is a hallmark of wound healing and cancer that is commonly attributed to myofibroblasts. However, it remains unknown which effect collagen microarchitecture has on myofibroblast differentiation. Here, we combined experimental and computational approaches to investigate the hypothesis that the microarchitecture of fibrillar collagen networks mechanically regulates myofibroblast differentiation of adipose stromal cells (ASCs) independent of bulk stiffness. Collagen gels with controlled fiber thickness and pore size were microfabricated by adjusting the gelation temperature while keeping their concentration constant. Rheological characterization and simulation data indicated that networks with thicker fibers and larger pores exhibited increased strain-stiffening relative to networks with thinner fibers and smaller pores. Accordingly, ASCs cultured in scaffolds with thicker fibers were more contractile, expressed myofibroblast markers, and deposited more extended fibronectin fibers. Consistent with elevated myofibroblast differentiation, ASCs in scaffolds with thicker fibers exhibited a more proangiogenic phenotype that promoted endothelial sprouting in a contractility-dependent manner. Our findings suggest that changes of collagen microarchitecture regulate myofibroblast differentiation and fibrosis independent of collagen quantity and bulk stiffness by locally modulating cellular mechanosignaling. These findings have implications for regenerative medicine and anticancer treatments.

collagen microarchitecture | myofibroblast differentiation | 3D fibrous matrix mechanics | mechanosignaling | adipose-derived stem cells

Myofibroblasts are key players of both physiological and pathological tissue remodeling. During normal wound healing, α-smooth muscle actin (α-SMA)-positive myofibroblasts deposit and remodel extracellular matrix (ECM) and secrete proangiogenic factors that collectively enable the formation of new granulation tissue (1, 2). Upon resolution of inflammation, this myofibroblast-mediated stromal reaction typically disappears. However, persistent activation of myofibroblasts leads to pathological fibrosis and tissue stiffening, which can impair organ functions (e.g., myocardial and liver fibrosis) and limit the success of regenerative therapies (3–5). Additionally, persistent activation of myofibroblasts aggravates tumorigenesis due to ECM remodeling and altered paracrine functions (6, 7), and similar mechanisms contribute to the observation that certain preconditions (e.g., obesity) are linked epidemiologically with increased cancer risk and worse prognosis (8–10). Therefore, gaining an improved understanding of the molecular and biophysical signals that contribute to myofibroblast activation and consequential changes in ECM remodeling and vascular responses will be critical.

Various biochemical factors such as transforming growth factor-β1 (TGF-β1) have been identified as key mediators of myofibroblast differentiation and fibrosis (1, 11), yet ECM-mediated biophysical cues can be equally important (1, 12–15). Indeed, previous reports have demonstrated that substrate stiffnesses characteristic of tumors or fibrotic tissue can trigger myofibroblast proliferation and differentiation independent of biochemical cues (13–16). While these studies have yielded important insights, they were performed on two-dimensional (2D), nonfibrous, and purely elastic polyacrylamide (PA) gels (13, 14, 16). In contrast, native ECM consists of fibrous networks that exhibit viscoelastic rather than elastic properties and thus can adjust their mechanical properties in response to cell-mediated stresses (17–20). Importantly, an increasing number of studies suggests that ECM viscoelasticity, nonlinear elasticity, and fiber rearrangement are key regulators of cell spreading, proliferation, and multilineage differentiation, and that the specific biophysical properties of substrate fibers contribute to this process (21–26). Consequently, examining myofibroblast differentiation as a function of varying bulk elastic moduli in nonfibrous PA gels may not fully recapitulate the signaling mechanisms, and thus fate decisions that cells explore as they engage with native ECM.

Type I collagen is the most abundant protein in native ECM and regulates wound healing and pathological fibrosis partly by

Significance

Pathologic fibrosis is associated with altered collagen microarchitecture, but the functional impact of these changes on myofibroblast differentiation remains poorly understood. We experimentally and computationally analyzed the effect of collagen microstructure on matrix mechanics and determined its functional consequences on adipose-derived stem cells (ASCs), a cell type contributing to obesity- and cancer-associated fibrosis. Our findings highlight that collagen networks with thicker fibers and larger pores exhibit higher shear moduli than their similarly concentrated counterparts with thinner fibers and smaller pores. These differences promoted ASC mechanosignaling and consequential differentiation into α-smooth muscle actin-positive, contractile, and proangiogenic myofibroblasts. Insights from this work will advance the design of biomaterials for tissue engineering applications as well as antifibrotic therapies.

Author contributions: B.R.S., X.C., D.G., V.B.S., and C.F. designed research; B.R.S., X.C., L.L., Y.H.S., A.A.S., S.C., and J.G. performed research; K.W., R.C.A.E., D.G., and V.B.S. contributed new reagents/analytic tools; B.R.S., X.C., L.L., Y.H.S., A.A.S., S.C., J.G., J.S., D.G., and C.F. analyzed data; B.R.S., X.C., and C.F. wrote the paper; and D.G., V.B.S., and C.F. provided feedback and insights.

The authors declare no competing interest.

This article is a PNAS Direct Submission.

[1]To whom correspondence may be addressed. Email: cf99@cornell.edu.

This article contains supporting information online at https://www.pnas.org/lookup/suppl/doi:10.1073/pnas.1919394117/-/DCSupplemental.

determining the structural and mechanical properties of the ECM (27–31). For example, increased collagen fiber thickness and alignment are indicative of a tumor-promoting stroma and correlate with increased cancer invasion and malignancy (8, 29, 32–34). Additionally, different types of scarring (hypertrophic, normotrophic, or keloid scars) are associated with distinct collagen fiber microstructure (28), and increased collagen fiber diameter in the heart is linked with age-dependent changes of cardiovascular function (31). While these pathological changes are most commonly attributed to a collagen-dependent increase in bulk tissue stiffness, recent studies suggest that local ECM microarchitecture rather than bulk substrate elasticity determines cell behavior by activating a mechanical feedback loop (17, 35). Importantly, myofibroblasts are highly contractile cells, which drive collagen network remodeling (i.e., fiber alignment and densification) and thus contribute to the nonlinear elasticity of the ECM. However, it remains largely unknown whether collagen network architecture functions as an independent mechanoregulator of myofibroblast differentiation.

Here, we investigated the hypothesis that the microarchitecture of collagen networks controls myofibroblast differentiation by regulating cellular mechanosignaling independent of bulk stiffness. Three-dimensional (3D) collagen networks with two distinct microarchitectures, but constant concentration, were fabricated by adjusting the hydrogel casting temperature. Adipose stromal cells (ASCs) were used as representative cell type given their key role in breast cancer and obesity-associated fibrosis (8, 36, 37). Experimental and computational approaches were explored to characterize the mechanical properties of the different hydrogels and resulting cellular responses. These studies reveal mechanistic insights into the role of collagen network microarchitecture in fibrosis with implications for cancer, stem cell, and tissue engineering research.

Results

Fabrication of Collagen Scaffolds with Defined Microarchitecture. As the lateral growth of collagen fibrils is temperature dependent, adjusting the gelation temperature allows controlling collagen fiber diameter independent of chemical parameters such as adhesion ligand density (23, 38–40). Here, we adapted this strategy for use in microfabricated polydimethylsiloxane (PDMS) microwells to permit 3D culture studies without limitations in oxygen and nutrient supply that can be analyzed with advanced imaging approaches (41). PDMS microwells (50 μm in depth) were fabricated as previously described and equilibrated at 37 °C or 4 °C. Subsequently, neutralized collagen solutions were quickly gelled in prewarmed microwells at 37 °C (referred to as "warm-cast") or slowly gelled in precooled microwells by gradually increasing the temperature from 4 °C to 37 °C (referred to as "cold-cast") (Fig. 1*A*). Visualization of collagen microarchitecture using confocal reflectance microscopy (CRM) confirmed that warm-cast collagen gels consisted of networks with thin fibers and seemingly low porosity, whereas cold-cast scaffolds were composed of thicker collagen fibers with larger pores (Fig. 1*B*). For a more detailed structural analysis, scanning electron microscopy (SEM) was performed (Fig. 1*B*). SEM image analysis of network pore and fibril diameter using an erosion algorithm and an autocorrelation method, respectively (42), confirmed that cold-cast collagen scaffolds were composed of thicker fibers and larger pores compared to warm-cast scaffolds (Fig. 1 *C*, *i* and *ii*), consistent with previous reports and the CRM image analysis (38). Nevertheless, SEM sample preparation may lead to drying artifacts, and thus the values presented in Fig. 1 *C*, *i* and *ii*, should be interpreted as relative rather than absolute differences. Furthermore, CRM image analysis verified that the porous structure of the collagen scaffolds is homogeneous in each condition, but varies between conditions (Fig. 1 *C*, *iii*), and that the different gelation protocols did not affect fiber linearity (Fig. 1 *C*, *iv*). Finally, gelation of collagen gels with ASCs yielded similar differences in fiber and pore diameter, suggesting that this protocol can be applied to study the effect of the different network properties in the presence and absence of cells (*SI Appendix*, Fig. S1 *A* and *B*).

Experimental and Theoretical Analysis of Collagen Network Mechanical Properties. Next, we determined how the different fabrication techniques affected the mechanical properties of the collagen gels. Consistent with previous analyses of fibrotic tissues, we first analyzed

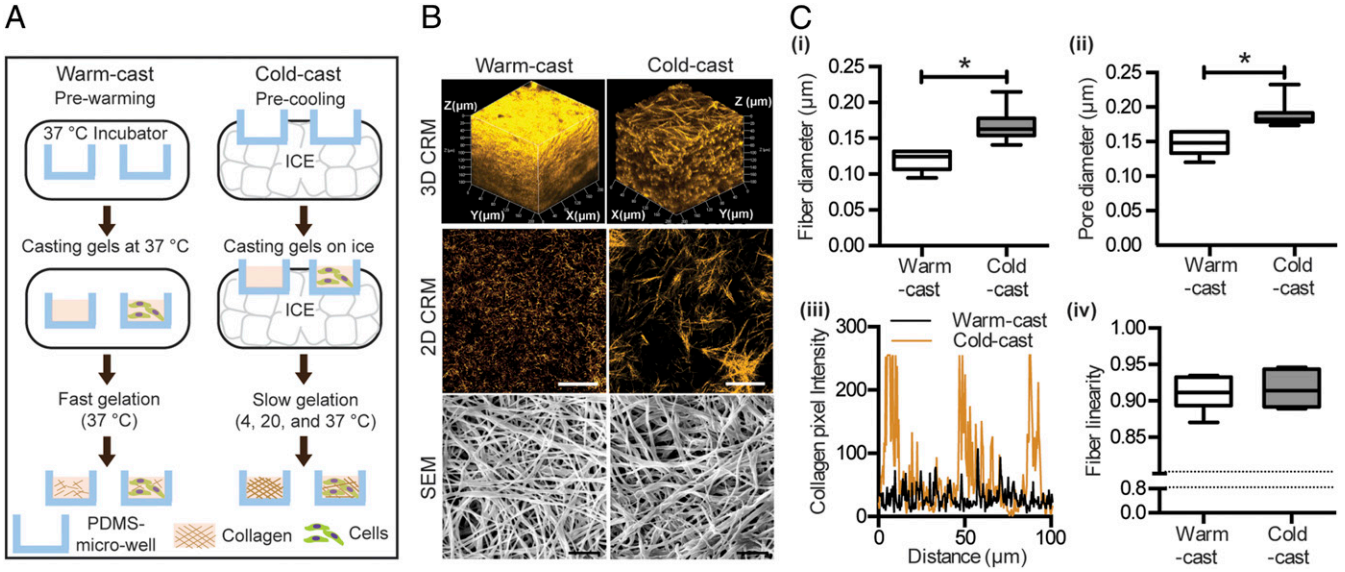

Fig. 1. Fabrication and characterization of collagen scaffolds with defined microarchitecture. (*A*) Schematic depicting the preparation of collagen hydrogels with controlled microarchitecture. (*B*) Confocal reflectance microscopy (CRM) and scanning electron microscopy (SEM) images of warm- and cold-cast collagen scaffolds (3D CRM, *z* stacks; 2D CRM, representative slice *z* stacks). (Scale bars: 50 μm for CRM and 1 μm for SEM.) (*C*) SEM image analysis of fiber and pore diameter (*i* and *ii*) as well as fiber linearity (*iv*). CRM image analysis showing the cross-sectional distribution of collagen fibers in a randomly selected location (*iii*). $*P < 0.05$ between conditions.

the elastic moduli of the differently structured gels using compression tests (36, 43). Neither dynamic mechanical thermal analysis (DMTA) nor atomic force microscopy (AFM)-based static indentation revealed differences in Young's modulus between cold- and warm-cast gels regardless of the presence of cells (*SI Appendix*, Fig. S2). However, both analyses assume elastic deformation, and static compression tests may primarily detect poroelastic effects (i.e., water migration out of the gels) (*SI Appendix*, Fig. S2 *A* and *B*), whereas cells frequently deform their ECM by applying tension and releasing stress by reorganizing their surrounding ECM (17, 22). Therefore, we next examined whether the fabrication-dependent changes in network structure modulate the rheological properties of collagen gels using both theoretical and experimental approaches.

When collagen gels are subjected to shear stress, a fraction of initially randomly oriented fibers starts to align along the direction of the principal stretch (tensile) resulting in a significant increase in stiffness and a nonlinear stress–strain relationship referred to as strain-stiffening (Fig. 2*A*) (17, 19, 44). To determine whether the different fabrication conditions affected the stress–strain relationship of collagen in our experimental setup, rheology testing was performed to probe the network shear moduli at different strain levels. Indeed, these experiments confirmed that both warm- and cold-cast gels stiffened when subjected to increased levels of strain. Interestingly, however, strain levels (~10%) comparable to cell-mediated remodeling yielded higher shear moduli in cold-cast relative to warm-cast scaffolds (Fig. 2*B*). These results suggest that cold-cast collagen gels exhibit higher shear moduli in physiologically relevant regimes relative to their warm-cast counterparts (Fig. 2*B*). To explore in more detail which specific structural properties of the two collagen constructs contributed to the observed differences, we used a theoretical model that captures the mechanical behavior of fibrous networks under loading (45). First, we confirmed that the model can fit the stress–strain relationship ($R^2 > 0.99$) similar to what we observed experimentally, validating its overall relevance to the specific context of this study (Fig. 2*B*). By fitting the experimental data, we found that the cold-cast scaffolds have higher shear moduli (at 1% shear strain) than their warm-cast counterparts (Fig. 2*C*). Additionally, our model has identified that the differently prepared networks started to stiffen at a similar critical strain ($\lambda_c \sim 1.02$), which is consistent with our rheology measurements where the slope of the stress–strain curves started to increase around 4% shear strain (corresponding with 2% tensile strain in the network) (Fig. 2*B*). This effect was more pronounced in cold-cast scaffolds ($E_f = 1{,}009.3 \pm 501.4$ Pa) as compared to warm-cast scaffolds ($E_f = 744.2 \pm 111.22$ Pa) according to our computational analysis of fiber modulus E_f (Table 1). This difference can in part be explained by the increased fiber thickness of cold-cast scaffolds (Fig. 1*C*) as the thickness of individual fibers directly correlates with their respective stiffness (23). In addition, the relatively larger pore size of cold-cast scaffolds increases the distance between each collagen cross-link, which promotes fiber buckling under shear loading. As buckled fibers provide less resistance to the realignment of stretched fibers, the cold-cast scaffolds can strain-stiffen more significantly compared to their warm-cast counterparts. DMTA and AFM-based static compression may not necessarily detect this difference because collagen fiber networks exhibit distinct mechanical behavior and reorganization (i.e., fiber bending vs. fiber buckling and alignment) when compressed vs. stretched and sheared (44). Collectively, these experimental and computational results suggest that increased collagen fiber thickness and network porosity facilitate fiber alignment and network stiffening in response to increased strain.

Effect of Collagen Microstructure on ASC Contractility and Mechanosignaling. Given that matrix mechanical properties can influence cellular mechanosignaling (17, 25), we next investigated whether the detected architecture-dependent changes of collagen network mechanics can stimulate integrin-dependent cell contractility. Such changes in cell contractility could activate a positive-feedback loop that further increases local collagen stiffness due to external tension on matrix fibers (*SI Appendix*, Fig. S3). We first utilized a mathematical model of cells embedded in a 3D matrix representing the cold-cast or warm-cast collagen networks (Fig. 3*A* and Table 2). In this model, we assume that a cell is of ellipsoidal shape and symmetric with respect to its long axis (Fig. 3 *A*, *i*). The cell is modeled as an active material (see *Materials and Methods* for details) that consists of a passive elastic component (representing the elasticity of the cytoskeleton) and an active component (representing the contractile forces generated by myosin motors). Also, the magnitude of ASC contractile forces was measured to be in the range of ~200 Pa on 2D substrates (46), which is similar to the contractility we assume in this *in silico* model. As we increase the aspect ratio of the cell while keeping the volume fixed, both the cell volumetric stress (σ_{kk}) and the deviatoric stress along the cell long axis ($\tilde{\sigma}_{33}$) increase. In response to the elevated stress, the cell recruits additional phosphorylated myosin motors through force-activated signaling pathways (e.g., Rho-ROCK, Ca^{2+}) and polarizes to form aligned contractile actin filaments, as indicated by the high levels of the mean contractility (ρ_{kk}) and its polarization along the long axis ($\tilde{\rho}_{33}$). With increased myosin recruitment and polarization, the cell active energy U_{cell}

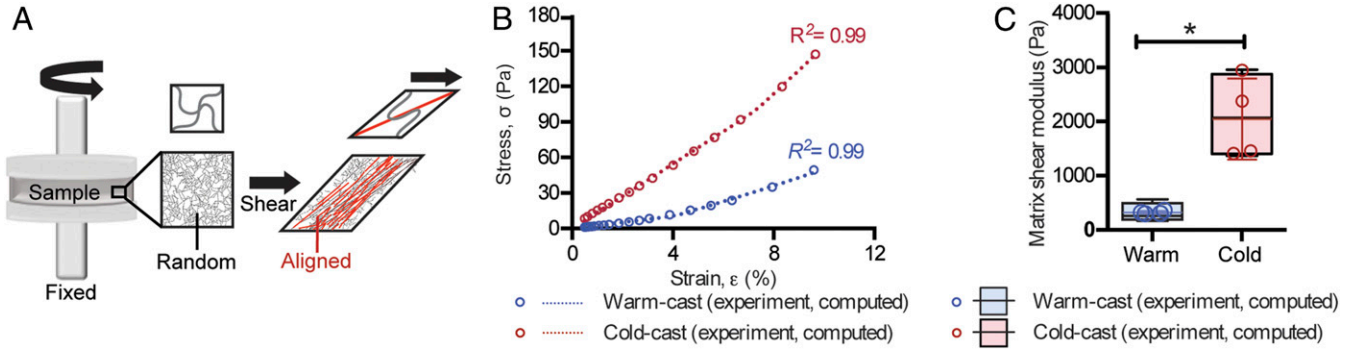

Fig. 2. Theoretical and experimental analysis of collagen mechanical properties. (*A*) Schematic illustrating the effect of shear stress on fiber alignment during rheology testing. A fraction of fibers aligns (red) with the first principal stretch direction leading to stiffening under loading. The fibers that do not align (black) remain randomly oriented and isotropic. (*B*) Representative stress–strain curves of cell-free cold- and warm-cast scaffolds as obtained by experimental analysis or computational simulation. (*C*) Average of shear moduli of cold- and warm-cast scaffolds obtained via rheological measurements and computational modeling. *$P < 0.05$ between conditions.

Table 1. The computed mechanical properties by fitting the stress and strain data obtained in rheological experiments

	Sample no.	μ_m, Pa	E_f, Pa	λ_c
Cold-cast	1	1,365.7	1,008.5	1.032
	2	1,505.8	1,513.5	1.001
	3	2,623.5	325.5	1.029
	4	2,956.8	1,189.6	1.033
Average		2,112.9	1,009.3	1.023
Warm-cast	1	256.3	625.4	1.017
	2	270.2	769.7	1.036
	3	166.6	885.8	1.017
	4	567.4	695.9	1.019
Average		315.2	744.2	1.022

becomes more negative as the cell elongates (Fig. 3*B*). In the matrix, the elongated cell most significantly deformed the matrix proximal to the cell tips due to its polarized contractility (Fig. 3 *A*, *ii*). As highly elongated cells are shown to significantly deform the matrix, there is an associated increase in the strain energy, U_{matrix}. This acts as an energetic penalty that prevents the cell from taking on extremely large aspect ratios (Fig. 3 *B*, *i*). Finally, the increase in interfacial energy, $U_{interface}$, shown in Fig. 3*B* is attributed to the increase of cell surface area, which scales both the integrin-collagen binding energy and the membrane tension (Eq. **15**). The surface area is lowest when the cell assumes a spherical shape (given a fixed volume). As a result, the overall interfacial energy increases with increasing cell aspect ratio as shown in Fig. 3 *B*, *ii*, acting as a further penalty to cell elongation. Thus, the cell active energy decreases with increasing cell aspect ratio, while both the matrix energy and the cell–matrix interfacial energy increase. This competition leads to a nonmonotonic profile of the overall cell free energy with respect to its shape. Increasing the cell aspect ratio initially leads to a lowering of the free energy, and a minimum free energy configuration corresponds to the optimum cell aspect ratio.

As the stiffer cold-cast matrix has a higher resistance against the contraction, the cells experience larger tensile stresses, which activate the mechanosensitive pathways (e.g., Rho-ROCK, Ca^{2+}) (*SI Appendix*, Fig. S3). This leads to higher levels of myosin phosphorylation and increased cell contractile stress (calculated as ρ_{kk}/ρ_0) (Fig. 3 *A*, *ii*). Furthermore, the increase in the volumetric and deviatoric part of the contractility tensor ρ_{kk} and $\tilde{\rho}_{33}$ (associated with increasing cell aspect ratio) is more pronounced on stiffer matrices. As illustrated in Fig. 3*C*, the cell active energy becomes more negative with increasing myosin recruitment and polarization (via Eq. 14). Thus, in the stiffer cold-cast matrices, the contribution of the cell active energy to the decision of cell shape becomes more significant, pushing the cell to adopt an elongated and more spread shape (Fig. 3*D*). To dissect the individual and combined effects of matrix strain-stiffening and contractility feedback on cell polarization in more detail, we predicted cell polarization (cell aspect ratio) in the presence and absence of either or both. Not surprisingly, cell polarization was highest when both the contractility feedback and the matrix strain-stiffening were present. When we removed matrix strain-stiffening, cell polarization decreased but was still substantial. In contrast, when we removed the contractility feedback, cell polarization became negligible (*SI Appendix*, Fig. S4), suggesting that the contractility feedback is indispensable for cell polarization, while the strain-stiffening of the matrix magnifies this effect.

We validated the computational simulations with experiments by culturing ASCs in the different collagen systems and analyzing their contractility and cell shape. Confocal image analysis of nuclei- and actin-labeled cells verified that ASC stress fibers are more pronounced in cold-cast relative to warm-cast hydrogels (Fig. 4 *A*, *i*). Furthermore, ASCs assumed more spread and elongated cell morphologies (Fig. 4 *A*, *ii* and *iii*) when cultured in cold- vs. warm-cast collagen, a finding that correlated with a trend toward increased levels of phosphorylated myosin light chain (p-MLC) per cell, an indicator of increased cell contractility (Fig. 4*B*). Importantly, cell contractility in cold-cast collagen gels resulted in collagen fiber densification and alignment in the direction of cell polarization and migration consistent with our predictions (Fig. 4*C*). Collectively, these data suggest that cold-cast collagen matrices with thicker fibers and larger pores exhibit increased stiffness in a physiologically relevant regime of strain. This in turn promotes cell contractility, local matrix remodeling, and consequential changes in mechanosignaling.

Effect of Collagen Microstructure on ASC Differentiation into Myofibroblasts. Enhanced actomyosin-mediated cell contractility is a key indicator of stromal cell mechanoactivation that can lead to increased ASC growth and differentiation into myofibroblasts (8). Because of these connections, we tested whether changes in collagen network architecture promote ASC growth and myofibroblast differentiation. Indeed, ASCs cultured in cold-cast collagen grew more and exhibited increased levels of the myofibroblast marker α-SMA compared to the same cells cultured in warm-cast scaffolds (Fig. 5 *A* and *B*). The pericyte marker desmin was not affected in these settings (*SI Appendix*, Fig. S5), suggesting that increased collagen strain-stiffening due to fabrication-dependent changes of collagen structure promoted ASCs differentiation toward a myofibroblastic rather than pericytic phenotype.

ECM remodeling is a hallmark of myofibroblasts that contributes to both physiologic and pathologic tissue remodeling and involves de novo deposition of the mechanosensitive ECM component fibronectin (Fn) (1, 49). More specifically, ASCs differentiated into myofibroblasts not only deposit more Fn but also change the conformation of the resulting Fn networks by partially unfolding individual fibers (50, 51). Furthermore, cells cultured on stiff PA gels deposit more extended Fn fibers relative to their counterparts cultured on soft gels (52). Given these reported links between Fn conformational changes, substrate mechanics, and cell contraction, we tested the hypothesis that cold-cast collagen hydrogels, which have increased strain-stiffening behavior relative to similarly concentrated warm-cast collagen networks lead to de novo deposition of more extended Fn fibers. To test this hypothesis, we utilized a previously described Förster resonance energy transfer (FRET) imaging technique to probe whether collagen network architecture modulates the conformation of newly deposited Fn (49–51). FRET-labeled, soluble Fn was supplemented to ASC cultures in cold- or warm-cast collagen gels to allow for its incorporation into newly deposited ECM. During the first 24 h of culture, collagen architecture did not affect the conformation of de novo deposited Fn as indicated by similar FRET intensities in warm- and cold-cast collagen gels (Fig. 5*C*). However, a significant decrease in FRET intensity after 48 h of culture suggested that ASCs in cold-cast gels deposit more extended Fn fibers relative to ASCs cultured in warm-cast scaffolds. Interestingly, this difference in cold-cast cultures was further enhanced after 72 h, whereas Fn matrices in warm-cast collagen cultures were characterized by increased FRET intensity indicative of a more folded Fn fiber state (Fig. 5*C*). These changes in Fn conformation were ASC dependent as incubation of cell-free collagen scaffolds with FRET-labeled Fn for similar periods of time did not yield a detectable FRET signal (*SI Appendix*, Fig. S6). Similarly, the architecture of the scaffolds did not change over time in the absence of cells (*SI Appendix*, Fig. S7), while ASCs remodeled their surrounding matrix in both cold- and warm-cast gels (*SI Appendix*, Fig. S1). Importantly, ASCs in cold-cast, but

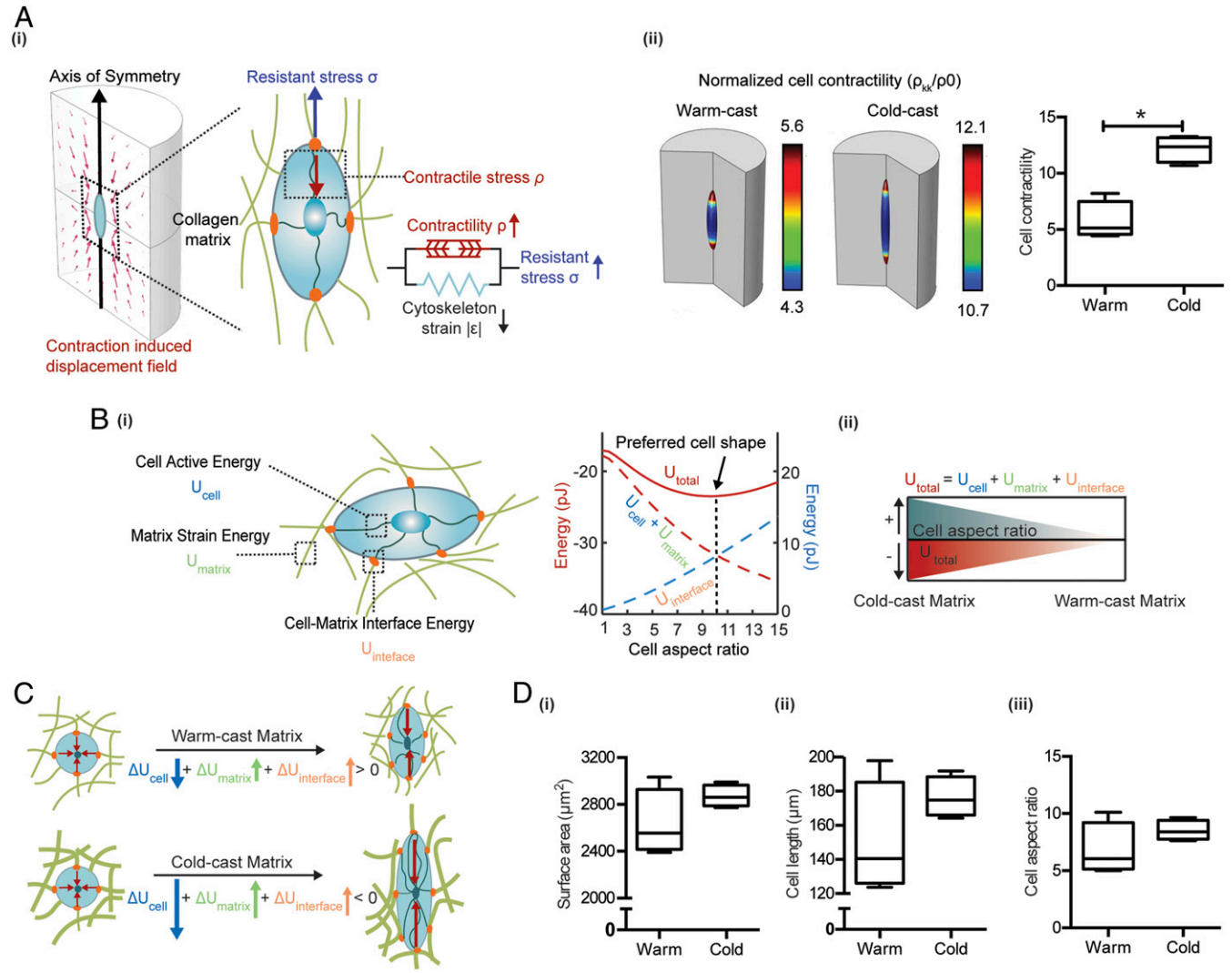

Fig. 3. Computational simulation of ASC behavior in response to altered collagen microarchitecture. (*A*, *i*) Mathematical model of cells in 3D matrix depicts the contractility and axis-symmetric shape of cells with respect to the long axis. Cells can exert contractile forces on the surrounding matrix, and the magnitude of such forces is dependent on the stress applied to the cell. (*ii*) Cell contractility is proportional to the phosphorylated myosin motor density in cold-cast and warm-cast collagen matrices predicted by the finite element model. (*B*, *i*) The minimum of U_{total} (total free energy of the system), which consists of U_{cell} (cell active energy), U_{matrix} (strain energy of matrix), and $U_{interface}$ (cell–matrix interface energy) indicates the preferred cell aspect ratio. The energy level plotted on the left *y* axis (red) is for U_{total}, U_{cell}, and U_{matrix}, and the one on the right *y* axis (blue) is the energy value of $U_{interface}$. (*ii*) The schematic summarizes the relationship between *U* total and cell aspect ratio. (*C*) In the cold-cast matrix, due to the increased stiffness, elongation is associated with a larger increase in the cell volumetric stress and actomyosin assembly. The reduction in the cell active energy favors elongation in the cold-cast matrices compared to the warm-cast matrices. (*D*) Prediction of cell (*i*) surface area, (*ii*) cell length, and (*iii*) cell aspect ratio in cold- and warm-cast collagen by the finite-element model.

not warm-cast gels decreased the pore diameter of the networks while increasing fiber linearity, and both changes are associated with increased cell contractility and synergistic to ECM stiffness (*SI Appendix*, Fig. S1 and Fig. 5 *B* and *C*) (17, 20, 45).

Another hallmark of myofibroblasts is their pronounced proangiogenic potential (2). Thus, we determined whether the detected collagen architecture-dependent changes in ASC myofibroblast differentiation coincide with increased secretion of two widely investigated proangiogenic factors, vascular endothelial growth factor (VEGF) and interleukin-8 (IL-8). Indeed, ASCs cultured in cold-cast scaffolds secreted greater amounts of VEGF and IL-8 than those cultured in warm-cast scaffolds (Fig. 5*D*). Collectively, these results indicate that collagen matrices with thicker fibers and increased pore size stimulate ASC differentiation into myofibroblasts and corresponding changes in ECM remodeling and proangiogenic factor secretion. It would be interesting to test in the future whether the positive-feedback loop between cell contractility and ECM remodeling/stiffening regulates ASC differentiation in a nonlinear manner over time and which timescales (hours [necessary for cell contractility buildup] (53) vs. days [necessary for ECM remodeling; Fig. 5*C*]) are most relevant to potentially interfere with this process therapeutically.

Collagen Microstructure Regulates ASC Myofibroblast Differentiation by Varying Cell Contractility. Next, it was our goal to confirm that the above-described phenotypic changes of ASCs are directly related to the increased strain-stiffening of cold-cast scaffolds and consequential changes in cell contractility. ASCs were cultured in cold- vs. warm-cast scaffolds with or without pharmacological inhibition of Rho-associated protein kinase (ROCK), a key regulator of mechanosignaling that controls actin filament

Table 2. Parameters used in the simulation

Parameters	Physical meaning	Values	Origin
ρ_0	Cell motor density (quiescent state)	0.1 kPa	Ref. 47
K	Cell bulk modulus	1,667 Pa	Ref. 47
μ	Cell shear modulus	1,250 Pa	Ref. 47
β	Cell chemical stiffness	2.77 kPa^{-1}	Ref. 47
α_d	Cell deviatoric feedback parameter	2.60 kPa^{-1}	Ref. 47
α_v	Cell volumetric feedback parameter	2.60 kPa^{-1}	Ref. 47
n	Fiber transition parameter	5	Ref. 45
m	Fiber stiffening parameter	10	Ref. 45
γ	Cell matrix adhesion energy	0.13 mJ/m^2	Ref. 48
V	Cell volume before contraction	31,400 μm^3	Fit to experiment

organization and contractility in part through phosphorylating MLC (54, 55). ROCK inhibition with Y27632 reduced α-SMA levels in both warm- and cold-cast collagen gels, but this trend was more pronounced in cold-cast collagen (Fig. 6*A*). Consistent with decreased myofibroblast differentiation, ROCK inhibition also reduced VEGF and IL-8 secretion by ASCs cultured in cold-cast collagen, but had no significant effect on VEGF and IL-8 secretion of ASCs cultured in warm-cast collagen (Fig. 6*B*). We also confirmed that the different angiogenic factor secretion was not primarily due to varied Fn deposition because Fn-deficient mouse embryonic fibroblasts (MEFs) secreted more VEGF in cold- vs. warm-cast collagen scaffolds (*SI Appendix*, Fig. S8). As inhibition of ROCK can affect cell behavior by mechanisms other than altered myosin phosphorylation (56), we also performed inhibition studies with blebbistatin, which blocks myosin II more directly. Similar to Y27632, blebbistatin treatment perturbed ASC morphology, actin stress fiber formation, and assembly of α-SMA fibers in cold-cast collagen (albeit levels of α-SMA protein were not significantly reduced) (*SI Appendix*, Fig. S9), confirming our conclusions. Last, we tested whether nuclear localization of the mechanosensitive transcription factor YAP (Yes-associated protein), which has been associated with myofibroblast differentiation (15, 57), was differentially affected by collagen microarchitecture. In contrast to 2D experiments where increased substrate stiffness increases YAP nuclear localization, ASCs exhibited reduced YAP nuclear localization in the stiffer cold- vs. softer warm-cast gels (*SI Appendix*, Fig. S10). Collectively, these data indicate that increased cell contractility is stimulating ASC myofibroblast differentiation and proangiogenic capability in cold-cast hydrogels relative to their warm-cast counterparts, but that YAP nuclear translocation is less critical for this process than in 2D culture.

ASCs Regulate Endothelial Sprouting as a Function of Collagen Microstructure. Given the reported links between myofibroblasts and increased vascularization (2, 11, 58), and our observation

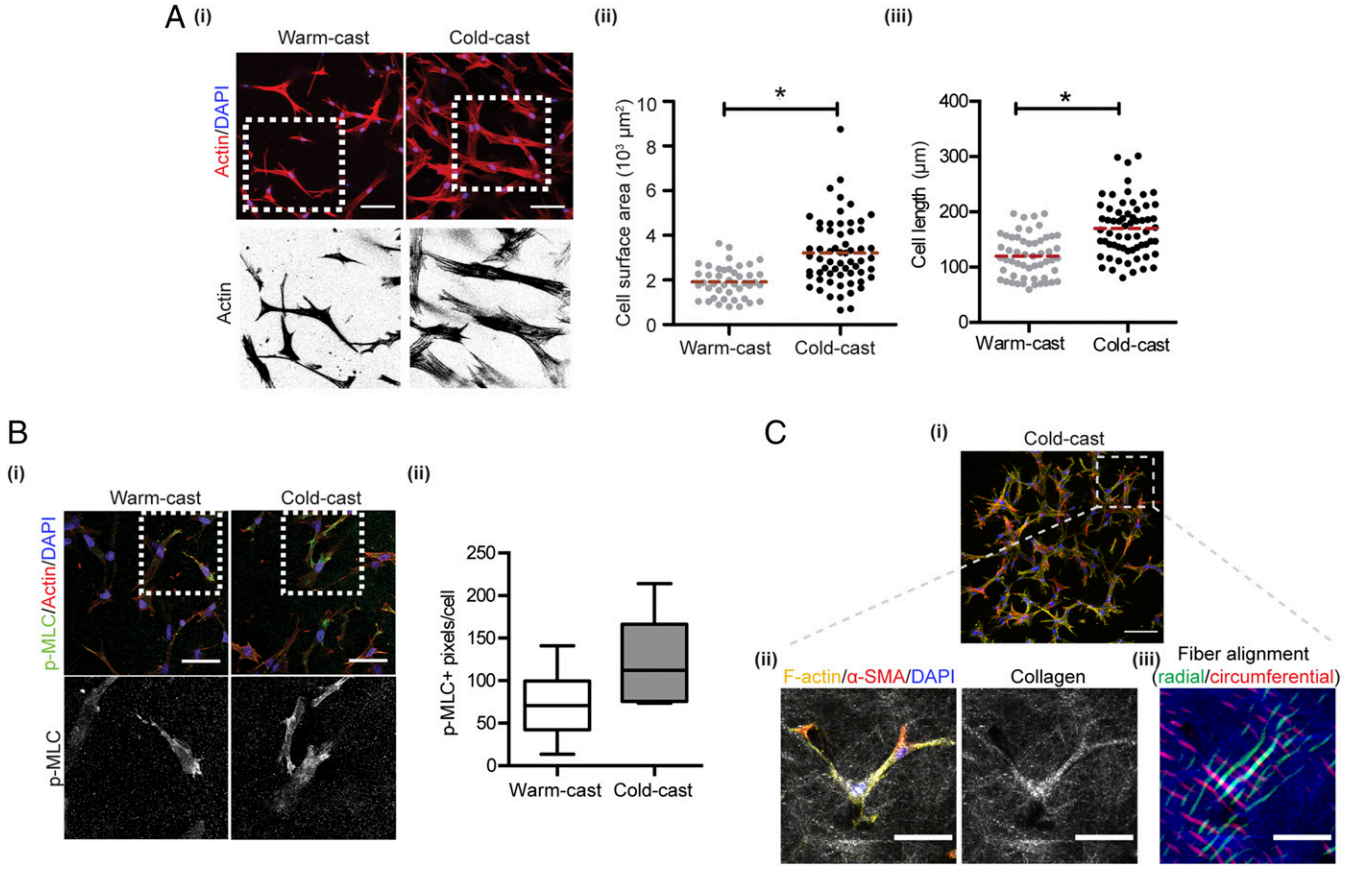

Fig. 4. Collagen microarchitecture regulates ASC morphology and contractility. (*A*) Confocal micrographs of cells stained for F-actin (red) and nuclei (blue) and corresponding image analysis of cell surface area (*ii*) and length (*iii*). (*B*) Confocal image analysis of p-MLC levels per cell in each condition. p-MLC (green), F-actin (red), and nuclei (blue). (Scale bars: 50 μm.) (*C*) Confocal IF (*i*) and CRM (*ii*) images of collagen fiber densification and alignment relative to cell spreading in cold-cast scaffolds. Collagen (white), α-SMA (red), F-actin (yellow), and nuclei (blue). (*iii*) Pseudocolored map of collagen fiber direction and alignment as determined by image analysis of CRM micrographs. Radial (green) and circumferential (red). (Scale bars: 100 μm for the *Top* image and 50 μm for the *Bottom* images.) $^*P < 0.05$.

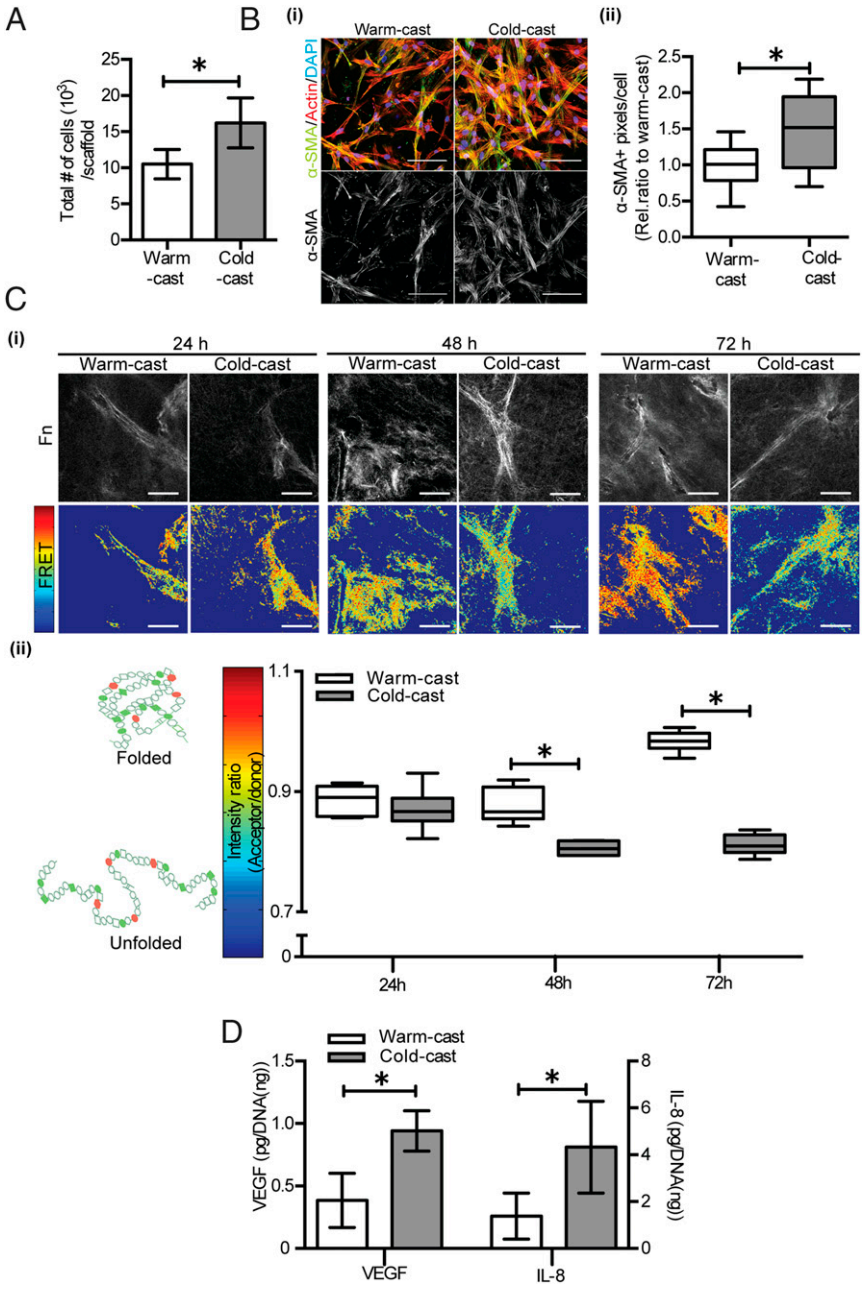

Fig. 5. Collagen microarchitecture controls ASC myofibroblast differentiation. (*A*) Total number of ASCs in each construct as determined by image analysis. (*B*) (*i*) Confocal micrographs of ASCs stained for α-SMA (green), F-actin (red), and nuclei (blue) and (*ii*) corresponding quantification of α-SMA levels in warm- and cold-cast collagen. (*C*) Analysis of fibronectin (Fn) deposition and conformation by FRET: (*i*) black-and-white images indicate total amounts of Fn, while color-coded FRET images indicate Fn conformational changes after 24, 48, and 72 h. (*ii*) Box-and-whisker plots showing the average FRET intensity obtained from multiple positions per sample. (Scale bar: 50 μm.) Cooler (blue) colors represent unfolded Fn, corresponding to lower FRET intensity (acceptor/donor), while warmer (red) colors indicate folded Fn with a higher FRET intensity. (*D*) VEGF and IL-8 secretion as determined by ELISA and normalized to DNA content. $*P < 0.05$.

that collagen microarchitecture modulates ASC proangiogenic factor secretion, we next tested whether cold-cast collagen gels stimulate endothelial cell invasion by modulating the proangiogenic capability of ASCs. For these experiments, we utilized a previously described microfabricated endothelial cell invasion assay (59, 60). Cold- and warm-cast scaffolds were preconditioned in PDMS microwells with or without ASCs for 6 d after a monolayer of human umbilical vein endothelial cells (HUVECs) was seeded on top of the hydrogels and allowed to invade over 4 d (Fig. 7 *A*, *i*). Immunofluorescence and confocal imaging of $CD31^+$ endothelial sprouts allowed visualizing and quantifying the sprouting behavior of HUVECs (green) as a function of the hydrogel bulk (Fig. 7 *A*, *ii*). In the absence of ASCs, cold-cast collagen scaffolds promoted HUVEC sprouting relative to their warm-cast counterparts, but the presence of ASCs significantly increased this difference (Fig. 7*B*). These results suggest that collagen network architecture can directly affect HUVEC sprouting, but that ASCs potentiate these effects. To test whether the observed differences in HUVEC invasion were mediated by different proangiogenic factor secretion of ASCs

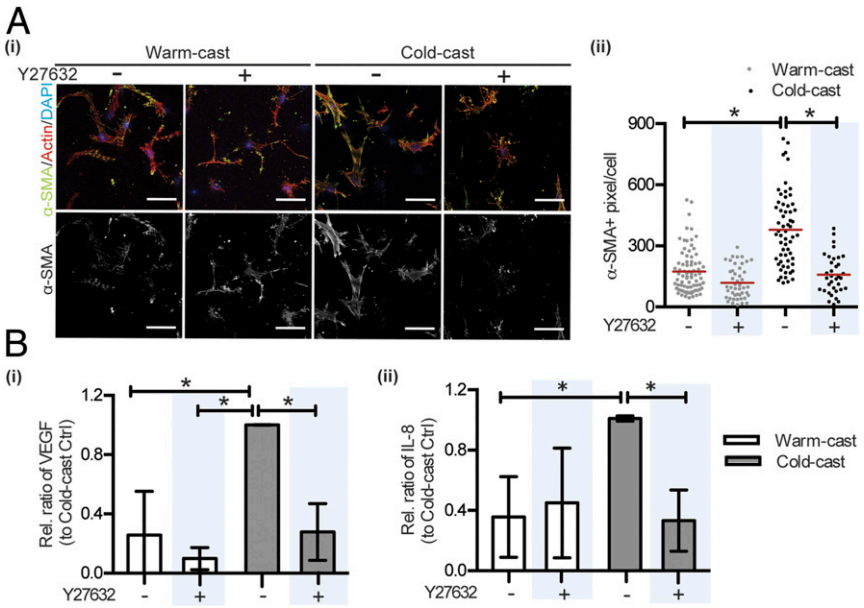

Fig. 6. Collagen microarchitecture regulates ASC myofibroblast differentiation and proangiogenic factor secretion by altering cell contractility. (*A*) Effect of Y27632 on collagen microarchitecture-dependent changes of α-SMA as determined by confocal image analysis. (*B*) Effect of Y27632 on collagen microarchitecture-dependent changes of VEGF and IL-8 secretion as determined by ELISA and normalized to DNA content. $*P < 0.05$.

between cold- vs. warm-cast scaffolds, we repeated these experiments in the presence and absence of function-blocking VEGF and IL-8 antibodies. Indeed, blockade of VEGF and IL-8 reduced HUVEC sprouting in cold-cast ASC cocultures to a level that was similar to warm-cast ASC cocultures. In contrast, no significant effect on sprouting was observed when VEGF and IL-8 were inhibited in ASC cocultures in warm-cast collagen (Fig. 7*C*). Importantly, inhibition of ASC contractility with Y27632 similarly suppressed HUVEC sprout formation in cold-cast ASC cocultures but had little effect in warm-cast ASC cocultures (Fig. 7*D*). Collectively, these data suggest that increased collagen fiber thickness and network porosity may promote angiogenic processes by stimulating ASC differentiation into proangiogenic myofibroblasts, and that changes in ASC mechanosignaling due to altered strain-stiffening may play a role in this process.

Discussion

While it is well established that myofibroblast differentiation impacts collagen microarchitecture, it is not clear which effect collagen microarchitecture has on myofibroblast differentiation. The experimental and theoretical results from our study suggest that cold-cast collagen networks with increased fiber thickness and pore size exhibit higher stiffness and more pronounced strain-stiffening relative to similarly concentrated warm-cast collagen gels composed of thinner fibers and smaller pores. Responding to the change in the network mechanics, ASCs embedded within cold-cast collagen developed a more contractile phenotype that mechanically triggered myofibroblast differentiation. Collagen microarchitecture-induced myofibroblast differentiation of ASCs altered ECM remodeling, and their contractility-dependent secretion of the proangiogenic factors VEGF and IL-8, in turn, promoted endothelial sprouting.

As the kinetics of collagen fibrillogenesis determine the microarchitecture of collagen (61–63), the latter can be adjusted by changing the pH, ionic strength, temperature, and macromolecular crowding (34, 38, 40). For the microscale culture experiments described herein, we varied fiber size by controlling the gelation temperature. Quick gelation at 37 °C yielded networks with thin fibers and small pores, while slow fibrillogenesis by gradually raising the gelation temperature from 4 to 37 °C generated networks consisting of larger fibers with increased pore sizes (Fig. 1). These microarchitectural changes influenced the mechanical behavior of each network. Experimental and computational analysis indicated that both collagen gels exhibited strain-stiffening regardless of fabrication temperature, but that cold-cast gels were stiffer compared to warm-cast scaffolds in response to shear loading (Figs. 2 and 3). The shear-mediated alignment of thicker collagen fibers in the direction of strain may influence the enhanced strain-stiffening of the cold-cast gels. In addition, this difference may be attributable to the fact that thicker fibers are stiffer than their thinner counterparts (35), but altered interfibrillar interactions may also contribute (64, 65).

Although increased cell contractility and mechanotransduction have previously been shown to induce myofibroblast differentiation as a function of bulk ECM concentration or elasticity (12–14), our results now suggest that changes in collagen network microstructure can induce similar effects. In our system, ASC-mediated contraction led to local collagen fiber alignment and compaction (as determined via increased fiber linearity and reduced pore size in the presence of ASCs) (Fig. 4*C* and *SI Appendix*, Fig. S1*B*), which collectively stiffened the matrix in these regions. This ASC contraction-mediated stiffening of local matrix, in turn, stimulated a contractile cell phenotype via a positive-feedback loop. The reciprocal between cellular contractility and matrix stiffness is essential to the polarization and elongation of the ASCs, and the stiffening of the matrix under contraction further magnifies the effect (*SI Appendix*, Fig. S4). Indeed, both our computational and experimental analysis verified that ASCs in cold-cast scaffolds were more contractile as indicated by increased cell spreading, p-MLC levels, and the inhibition of these effects by both Y27632 and blebbistatin, ultimately achieving an energetically favorable state of the system (Figs. 3, 4, and 6 and *SI Appendix*, Fig. S9). Our data also suggest that the interplay between cell active energy, matrix strain energy, and cell–matrix interface energy is key to mediating cell morphological changes. Increased cytoskeletal tension and contractility-mediated RhoA/ROCK can drive

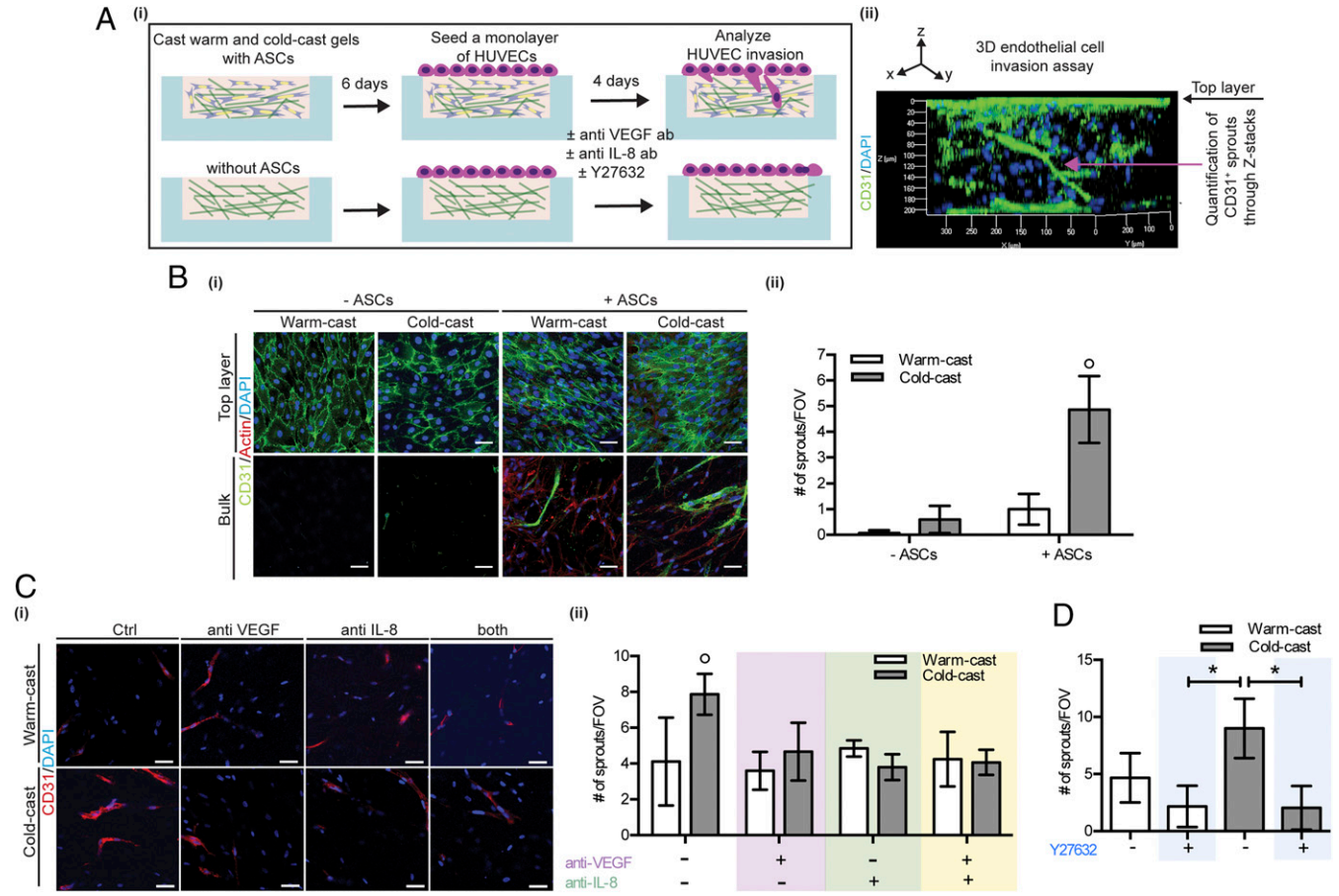

Fig. 7. Collagen microarchitecture controls endothelial sprouting by modulating ASC proangiogenic capability. (*A*, *i*) Schematic visualizing the experimental procedure to study human umbilical vein endothelial cell (HUVEC) invasion as a function of collagen-dependent changes of ASCs and (*ii*) representative 3D cross-sectional view of CD31-labeled HUVEC sprouting. (*B*, *i*) Representative confocal micrographs of CD31-labeled HUVEC monolayer (top layer) and HUVEC sprouts (bulk) for the different collagen conditions. (*ii*) HUVEC sprouts longer than 15 μm were quantified based on reconstructed IF *z* stacks. (Scale bar: 50 μm.) (*C*, *i* and *ii*) Representative confocal micrographs and quantification of HUVEC sprouts formed in warm- and cold-cast collagen with and without VEGF and/or IL-8 neutralizing antibodies. (Scale bars: 50 μm.) (*D*) Quantification of HUVEC sprouts in warm- and cold-cast collagen with and without Y27632 treatment. Data are represented as the number of sprouts per field of view (FOV) and its corresponding *Z* stack. The asterisk (*) and ○ indicate $P < 0.05$ between two and all other conditions, respectively.

myofibroblast differentiation (15), and the accompanying changes in matrix biophysical properties can further promote the phenotypic changes of ASCs (24). Our surprising result that YAP nuclear localization was not increased by cold-cast gels may be due to various reasons. For example, recent data suggest that mechanotransduction in 3D environments can occur independently of YAP (66). Moreover, YAP nuclear localization and activity is impacted by many other parameters not only substrate mechanics including actin integrity rather than Rho/ROCK mediated-myosin II contractility and changes in cell density (67, 68). Finally, it is possible that the kinetics of nuclear localization vary in warm- and cold-cast gels and that other mechanosensitive transcription factors such as myocardin-related transcription factor-A (MRTF-A) and its cofactor, serum response factor (SRF), for myofibroblast differentiation are similarly affected (13, 14, 69). Whether or not these signaling mechanisms contributed to collagen microarchitecture-dependent differentiation of ASC into myofibroblast will need to be tested in the future.

We have previously shown that collagen biophysical properties can directly affect vasculogenesis in an IL-8– and VEGF-dependent manner (70), but the results presented here suggest that indirect effects mediated by collagen structure-dependent changes of stromal cells have a more pronounced effect (Fig. 7). Several factors may have contributed to these findings. First, increased matrix stiffness can activate nuclear factor κB (NF-κB) (71), which stimulates transcription of IL-8 (71, 72), and IL-8 can stimulate VEGF bioactivity (73). Additionally, the detected Fn conformational changes could have contributed to increased VEGF secretion (51) and/or retention of matrix-binding proangiogenic factors (74). However, culturing Fn-deficient MEFs in cold- vs. warm-cast collagen still resulted in enhanced VEGF secretion (*SI Appendix*, Fig. S8). Furthermore, analysis of matrix-bound VEGF showed no differences between both conditions (*SI Appendix*, Fig. S11). Therefore, we concluded that altered Fn deposition may have been a modulating, but not the primary driver of the observed changes.

Nevertheless, other ASC-dependent changes of ECM remodeling could also play a role. For example, ASCs promote endothelial cell invasion of collagen by forming physical guidance channels via metalloproteinase (MMP)-dependent proteolytic degradation of the surrounding ECM (59). Interestingly, MMP bioactivity of stromal cells is both stiffness dependent (75) and contributes to increased pericellular stiffness (76). Furthermore, MMPs mediate the release of proangiogenic factors sequestered within the ECM (77). Therefore, it is possible that altered collagen microarchitecture promoted the proangiogenic capability of ASCs not only by increasing their secretion of VEGF and IL-8, but

varied MMP activity could have contributed as well. It should also be considered that microarchitecture-dependent differences in cell-mediated collagen fiber alignment and densification will change the concentration of locally available adhesion sites over time, which can independently affect cell behavior. Last but not least, collagen strain-stiffening in the context of pathological fibrosis is affected by many additional parameters including collagen concentration (17, 23). As such, future studies will be necessary to dissect how changes in collagen network microarchitecture modulate the synergistic interplay between ECM mechanical and chemical cues.

Collectively, our findings indicate that changes of collagen network microarchitecture mechanically modulate the reciprocal interactions between cells and their surrounding ECM independent of bulk tissue stiffness with functional consequences on both physiological and pathological tissue remodeling. For example, the abnormal collagen microarchitecture associated with aberrant scarring may not only be a consequence of dysfunctional wound healing but may in fact further stimulate scarring by promoting a myofibroblast differentiation (28). Moreover, increased breast tissue density is well known to be positively correlated with breast cancer risk and aggression (78). However, in older women the risk to develop breast cancer is significantly increased despite the fact that they tend to have less dense and more compliant breast tissue (79). Our data may help to explain this apparent contradiction: Breast tissue of older women often contains disorganized collagen fibers, which cannot be detected via routine bulk tissue measurements performed in the clinic (80). However, these microstructural changes modulate the physicochemical properties of the local matrix with functional consequences on mechanosignaling that may ultimately increase breast cancer risk and aggression. Future studies testing the role of collagen microarchitecture under conditions of increased ECM complexity (e.g., in the presence of other ECM components known to be involved in cancer such as laminin and hyaluronan) will be needed to more comprehensively evaluate these connections. Furthermore, in vivo studies will be necessary to determine the functional relevance of our data and potential implications for therapeutic approaches. In summary, our data expand knowledge of how biophysical and biochemical factors interface during health and disease and inform the design of collagen-based or collagen-mimetic systems for basic research, drug evaluation, and tissue engineering application.

Materials and Methods

Cell Culture. Human adipose-derived stem cells (ASCs) and HUVECs (both from Lonza) were cultured in ADSC-GM supplemented by growth factors (Lonza) and HUVEC-GM containing Bio-Whittaker medium 199 (M199; Lonza) with Endothelial Cell Growth Supplement (Millipore), 2 mM Glutamax, 5 U/mL heparin, 20% FBS (Tissue Culture Biologicals), and 1% penicillin/streptomycin (Gibco), respectively. Fn-null MEFs were generously provided by the Hocking Lab (University of Rochester, Rochester, NY) and cultured on 50 μg/mL collagen I (Gibco)-coated culture plates in Fn- and serum-free media using a 1:1 mixture of Cellgro (Mediatech) and Aim V (Invitrogen).

Preparation of Microfabricated Collagen Scaffolds with Varying Microstructure. Three-dimensional microwells were fabricated using PDMS Sylgard 184 silicone elastomer kit (Dow Corning) on a lithographically patterned silicon master containing circular patterns of 4 mm in diameter and 200 μm in height (59, 60). The surface of the microwells was treated with air plasma (Harrick Plasma), followed by 1% (vol/vol) poly-ethylenimine (Sigma-Aldrich), 0.1% (vol/vol) glutaraldehyde (Fisher Scientific), and then extensive washes to remove unreacted glutaraldehyde and covalently couple collagen to the microwell. Collagen was obtained by acid extraction of rat-tail tendon (Pel-Freez Biologicals) and reconstituted in 0.1% (vol/vol) acetic acid to a final concentration of 15 mg/mL (59, 60). The reconstituted collagen was neutralized with NaOH and mixed with ASCs to a final density of 2 million cells per mL in 0.6% collagen. Half of the suspension was placed into the prechilled microwells and slowly gelled by gradually changing temperature from 4 °C (10 min) to 20 °C (10 min) to 37 °C (10 min) to create thicker collagen fibrils, while the other half was solidified in prewarmed microwells at 37 °C (30 min). Following gelation, ASCs in the collagen scaffolds were cultured in growth media for up to 6 d.

Computational Analysis of Matrix and Cell Characteristics.

Fibrous constitutive model for the ECM. When the matrix is deformed, a fraction of the initially randomly oriented fibers aligns along the directions in which the principal stretches are tensile. This leads to an increase in matrix stiffness anisotropically along those directions. Other fibers remain unaligned and exhibit isotropic mechanical behavior. To capture the presence of these two distinct families of aligned and unaligned fibers, following our previous work, we write the overall strain energy of the matrix W_{ECM} as a summation of two contributions:

$$W_b = \frac{\mu_m}{2}\left(\overline{I_1} - 3\right) + \frac{K_m}{2}(J-1)^2, \quad [1]$$

$$W_f = \sum_{a=1}^{3} f(\lambda_a). \quad [2]$$

Here, W_b and W_f denote the strain energy density of the unaligned and aligned fibers, respectively; K_m and μ_m denote the bulk and shear moduli of the unaligned fibers, respectively. λ_1, λ_2, and λ_3 are the stretches in the three principal directions. $\overline{I_1}$ and J are defined as follows:

$$J = \det(F_{ij}), \quad [3]$$

$$\overline{I_1} = \left(\lambda_1^2 + \lambda_2^2 + \lambda_3^2\right)/J^{2/3}, \quad [4]$$

where F_{ij} is the deformation gradient tensor. The strain energy density function $f(\lambda_a)$ is defined by the following:

$$\frac{\partial f}{\partial \lambda_a} = \begin{cases} 0, & \lambda_a < \lambda_l \\ \dfrac{E_f\left(\dfrac{\lambda_a - \lambda_l}{\lambda_u - \lambda_l}\right)^n (\lambda_a - \lambda_l)}{n+1}, & \lambda_l \le \lambda_a < \lambda_u \\ E_f\left[\dfrac{\lambda_u - \lambda_l}{n+1} + \dfrac{(1+\lambda_a-\lambda_u)^{m+1}-1}{m+1}\right], & \lambda_a \ge \lambda_u, \end{cases} \quad [5]$$

where E_f, n, and m are material properties characterizing the stiffening behavior in response to tensile stresses. In this study, we let $\lambda_l = \lambda_c - (\lambda_c - 1)/8$ and $\lambda_u = \lambda_c + (\lambda_c - 1)/8$, where λ_c is the critical stretch corresponding to the onset of the strain-stiffening. Similar to the strain energy, the total stress σ_{ij} can be divided into the unaligned fiber response σ_{ij}^b and aligned fiber response σ_{ij}^f,

$$\sigma_{ij} = \sigma_{ij}^b + \sigma_{ij}^f, \quad [6]$$

which can be calculated from Eqs. 1, 2, and 5,

$$\sigma_{ij}^b = K_m(J-1)\delta_{ij} + \frac{\mu_m\left(B_{ij} - \frac{1}{3}B_{kk}\delta_{ij}\right)}{J^{5/3}}, \quad [7]$$

$$\sigma_{ij}^f = \frac{1}{J}\sum_{a=1}^{3} \frac{\partial f}{\partial \lambda_a}\lambda_a n_i^a n_j^a. \quad [8]$$

Here, n^1, n^2, n^3 are the unit vectors along the three principal directions, and B is the left Cauchy–Green tensor, defined as follows:pt

$$B_{ij} = F_{ik}F_{jk}. \quad [9]$$

Chemomechanical feedback model for cell contractility. Following our previous work (47), we model the cells using a combination of passive mechanical and active chemomechanical components (Fig. 3). The passive component represents the elasticity of the cytoskeleton, while the active component represents the contractile forces generated by phosphorylated myosin motors. The stress in the cell can be related to the strain using the strain such that

$$\sigma_{ij} = \left(\overline{\rho_0} + \overline{K}\varepsilon_{kk}\right)\delta_{ij} + 2\overline{\mu}\left(\varepsilon_{ij} - \frac{1}{3}\varepsilon_{kk}\delta_{ij}\right). \quad [10]$$

Here, σ_{ij} and ε_{ij} denote the stress and strain tensor. $\overline{\rho_0}$, $\overline{K}$, and $\overline{\mu}$ are three parameters, which can be calculated by the following:

$$\overline{\rho_0} = \frac{\beta\rho_0}{\beta - \alpha_v}, \quad \overline{K} = \frac{3K\beta - 1}{3(\beta - \alpha_v)}, \quad \overline{\mu} = \frac{2\mu\beta - 1}{2(\beta - \alpha_d)}. \qquad [11]$$

In the above equations, ρ_0 denotes the myosin motor density when the cell is in a stress-free quiescent state, K and μ denote the bulk modulus and shear modulus of the cell, β denotes the chemical stiffness, and α_v and α_d denote the volumetric and deviatoric chemomechanical feedback parameters. The parameters β and α are related to the molecular mechanisms that regulate the engagement of motors and stress-dependent signaling pathways. When the chemical stiffness β is small, α_v and α_d are large, the cell can recruit more myosin motors in response to the same level of external stress. The contractility tensor can be calculated as follows:

$$\rho_{ij} = \sigma_{ij} - \left(K\varepsilon_{kk}\delta_{ij} + 2\mu\left(\varepsilon_{ij} - \frac{1}{3}\varepsilon_{kk}\delta_{ij}\right)\right). \qquad [12]$$

The total free energy of the system can be calculated by the following:

$$U_{total} = U_{cell} + U_{matrix} + U_{interface}. \qquad [13]$$

In addition,

$$\begin{aligned} U_{cell} + U_{matrix} = \iiint \Bigg(& \frac{K}{2}(\varepsilon_{kk})^2 + \mu\tilde{\varepsilon}_{ij}\tilde{\varepsilon}_{ij} - \frac{1}{3}\int_0^{\varepsilon_{kk}} \sigma_{kk} d\varepsilon_{kk} - \int_0^{\tilde{\varepsilon}_{ij}} \tilde{\sigma}_{ij} d\tilde{\varepsilon}_{ij} \\ & + \frac{\beta}{6}(\rho_{kk} - 3\rho_0)^2 + \frac{\beta}{2}\tilde{\rho}_{ij}\tilde{\rho}_{ij} - \frac{1}{3}\int_0^{\rho_{kk}} \alpha_v \sigma_{kk} d\rho_{kk} - \int_0^{\tilde{\rho}_{ij}} \alpha_d \tilde{\sigma}_{ij} d\tilde{\rho}_{ij} \\ & + \frac{1}{3}\rho_{kk}\varepsilon_{kk} + \tilde{\rho}_{ij}\tilde{\varepsilon}_{ij}\Bigg) dV_{cell} + \iiint W_{ECM} dV_{matrix}. \end{aligned} \qquad [14]$$

Here, $\tilde{\rho}_{ij}$, $\tilde{\varepsilon}_{ij}$ and $\tilde{\sigma}_{ij}$ represent the deviatoric part of the contractility, strain, and stress tensors. V_{matrix} and V_{cell} denote the volume of matrix and cell, respectively. The cell–matrix free energy can be calculated by the following:

$$U_{interface} = \gamma S, \qquad [15]$$

where S is the surface area of the ellipsoid cell and γ is the cell–matrix interface energy density.

Table of the parameters. See Table 2.

Shear Modulus Analysis of 3D Collagen Matrix. Rheological experiments were performed on a DHR3 rheometer (TA Instruments) with built-in temperature and gab calibration. A 20-mm top- and bottom-plate geometry with a gap of 500 μm was used to measure the stress of the different collagen gels as a function of strain. To prevent handling-mediated defects in compliant collagen gels, which potentially alter the mechanical properties of the gels, collagen gels were fabricated in the rheometer. To prevent slippage of the collagen gels during the measurements, a glass coverslip treated with polyethylenimine followed by glutaraldehyde was glued to the bottom plate of rheometer. Subsequently, a neutralized collagen solution was injected and allowed to gel on the top of the coverslip. The collagen solution confined between the two plates of the rheometer was sealed by mineral oil to prevent evaporation and incubated for different durations at different temperature as described in *Materials and Methods*. For stress–strain measurements, we applied constant strains at a shear rate of 5.0×10^{-5} (1/s) until stress reached a yield strength at which the curve levels off.

Statistical Analysis. Student's *t* tests and ANOVA followed by Tukey's post hoc test were used to determine statistical difference between two conditions and among multiple conditions, respectively. Two-sided testing was performed for each analysis, and a *P* value less than 0.05 was considered statistically significant. When necessary, the data were log transformed and statistical analysis was performed based on the log-transformed data. All tests were performed on Microsoft Excel and GraphPad Prism 5. Unless otherwise noted, the mean ± SD is reported.

Data Availability. All data associated with the manuscript are provided within the manuscript.

ACKNOWLEDGMENTS. We thank Dr. Denise Hocking for generously providing Fn-null MEFs, Dr. Rebecca Williams for help with analysis of collagen fiber linearity, and Dr. Peter DelNero, Dr. Michael McCoy, Dr. Katharina Franziska Wittmann, and Dr. Luo Gu for helpful feedback on our manuscript. We also acknowledge funding from NIH/National Cancer Institute (NCI) (the Cornell Center on the Microenvironment and Metastasis through Award U54CA143876; the Cornell Center on the Physics of Cancer Metabolism through Award 1U54CA210184-01; Grants R01CA185293, 1S10RR025502-01, NYSTEM C029155, and NIH S10OD018516 for the imaging facilities of Cornell's Biotechnology Resource Center; and Grant DMR-1120296 for the Cornell Center for Materials Research Shared Facilities). Computational work was supported by NCI Awards (U01CA202177, U54CA193417, and R01CA232256), National Institute of Biomedical Imaging and Bioengineering Award R01EB017753, and the National Science Foundation Center for Engineering Mechanobiology (CMMI-154857). The content is solely the responsibility of the authors and does not necessarily represent the official views of the NCI or NIH.

1. J. J. Tomasek, G. Gabbiani, B. Hinz, C. Chaponnier, R. A. Brown, Myofibroblasts and mechano-regulation of connective tissue remodelling. *Nat. Rev. Mol. Cell Biol.* **3**, 349–363 (2002).
2. S. Vong, R. Kalluri, The role of stromal myofibroblast and extracellular matrix in tumor angiogenesis. *Genes Cancer* **2**, 1139–1145 (2011).
3. C. Y. Ho *et al*., Myocardial fibrosis as an early manifestation of hypertrophic cardiomyopathy. *N. Engl. J. Med.* **363**, 552–563 (2010).
4. A. Alam, K. Chun Suen, D. Ma, Acute-on-chronic liver failure: Recent update. *J. Biomed. Res.* **31**, 283–300 (2017).
5. R. B. Mannon, Therapeutic targets in the treatment of allograft fibrosis. *Am. J. Transplant.* **6**, 867–875 (2006).
6. A. Orimo *et al*., Stromal fibroblasts present in invasive human breast carcinomas promote tumor growth and angiogenesis through elevated SDF-1/CXCL12 secretion. *Cell* **121**, 335–348 (2005).
7. J. G. Goetz *et al*., Biomechanical remodeling of the microenvironment by stromal caveolin-1 favors tumor invasion and metastasis. *Cell* **146**, 148–163 (2011).
8. B. R. Seo *et al*., Obesity-dependent changes in interstitial ECM mechanics promote breast tumorigenesis. *Sci. Transl. Med.* **7**, 301ra130 (2015).
9. J. E. Druso, C. Fischbach, Biophysical properties of extracellular matrix: Linking obesity and cancer. *Trends Cancer* **4**, 271–273 (2018).
10. D. F. Quail, A. J. Dannenberg, The obese adipose tissue microenvironment in cancer development and progression. *Nat. Rev. Endocrinol.* **15**, 139–154 (2019).
11. Y. H. Song *et al*., Breast cancer-derived extracellular vesicles stimulate myofibroblast differentiation and pro-angiogenic behavior of adipose stem cells. *Matrix Biol.* **60–61**, 190–205 (2017).
12. F. Calvo *et al*., Mechanotransduction and YAP-dependent matrix remodelling is required for the generation and maintenance of cancer-associated fibroblasts. *Nat. Cell Biol.* **15**, 637–646 (2013).
13. X. Huang *et al*., Matrix stiffness-induced myofibroblast differentiation is mediated by intrinsic mechanotransduction. *Am. J. Respir. Cell Mol. Biol.* **47**, 340–348 (2012).
14. M. K. Willer, C. W. Carroll, Substrate stiffness-dependent regulation of the SRF-Mkl1 co-activator complex requires the inner nuclear membrane protein Emerin. *J. Cell Sci.* **130**, 2111–2118 (2017).
15. B. Piersma *et al*., YAP1 is a driver of myofibroblast differentiation in normal and diseased fibroblasts. *Am. J. Pathol.* **185**, 3326–3337 (2015).
16. J. L. Balestrini, S. Chaudhry, V. Sarrazy, A. Koehler, B. Hinz, The mechanical memory of lung myofibroblasts. *Integr. Biol.* **4**, 410–421 (2012).
17. M. S. Hall *et al*., Fibrous nonlinear elasticity enables positive mechanical feedback between cells and ECMs. *Proc. Natl. Acad. Sci. U.S.A.* **113**, 14043–14048 (2016).
18. S. Nam, K. H. Hu, M. J. Butte, O. Chaudhuri, Strain-enhanced stress relaxation impacts nonlinear elasticity in collagen gels. *Proc. Natl. Acad. Sci. U.S.A.* **113**, 5492–5497 (2016).
19. Q. Wen, P. A. Janmey, Effects of non-linearity on cell-ECM interactions. *Exp. Cell Res.* **319**, 2481–2489 (2013).
20. Y. L. Han *et al*., Cell contraction induces long-ranged stress stiffening in the extracellular matrix. *Proc. Natl. Acad. Sci. U.S.A.* **115**, 4075–4080 (2018).
21. O. Chaudhuri *et al*., Hydrogels with tunable stress relaxation regulate stem cell fate and activity. *Nat. Mater.* **15**, 326–334 (2016).
22. B. M. Baker *et al*., Cell-mediated fibre recruitment drives extracellular matrix mechanosensing in engineered fibrillar microenvironments. *Nat. Mater.* **14**, 1262–1268 (2015).
23. J. Xie, M. Bao, S. M. C. Bruekers, W. T. S. Huck, Collagen gels with different fibrillar microarchitectures elicit different cellular responses. *ACS Appl. Mater. Interfaces* **9**, 19630–19637 (2017).
24. M. L. Daniel, W. Y. Wang, M. R. Smith, A. Shikanov, B. M. Baker, Fiber density modulates cell spreading in 3D interstitial matrix mimetics. *ACS Biomater. Sci. Eng.* **5**, 2965–2975 (2019).
25. R. K. Das, V. Gocheva, R. Hammink, O. F. Zouani, A. E. Rowan, Stress-stiffening-mediated stem-cell commitment switch in soft responsive hydrogels. *Nat. Mater.* **15**, 318–325 (2016).
26. K. H. Vining, A. Stafford, D. J. Mooney, Sequential modes of crosslinking tune viscoelasticity of cell-instructive hydrogels. *Biomaterials* **188**, 187–197 (2019).
27. P. Fratzl, ""Collagen: Structure and mechanics, an introduction"" in *Collagen Structure and Mechanics*, P. Fratzl, Ed. (Springer, 2008), pp. 1–13.
28. M. Xue, C. J. Jackson, Extracellular matrix reorganization during wound healing and its impact on abnormal scarring. *Adv. Wound Care* **4**, 119–136 (2015).
29. P. P. Provenzano *et al*., Collagen reorganization at the tumor-stromal interface facilitates local invasion. *BMC Med.* **4**, 38 (2006).

30. K. R. Levental *et al*., Matrix crosslinking forces tumor progression by enhancing integrin signaling. *Cell* **139**, 891–906 (2009).
31. C. R. Gazoti Debessa, L. B. Mesiano Maifrino, R. Rodrigues de Souza, Age related changes of the collagen network of the human heart. *Mech. Ageing Dev.* **122**, 1049–1058 (2001).
32. M. W. Conklin *et al*., Aligned collagen is a prognostic signature for survival in human breast carcinoma. *Am. J. Pathol.* **178**, 1221–1232 (2011).
33. A. Ray, Z. M. Slama, R. K. Morford, S. A. Madden, P. P. Provenzano, Enhanced directional migration of cancer stem cells in 3D aligned collagen matrices. *Biophys. J.* **112**, 1023–1036 (2017).
34. J. Sapudom *et al*., The phenotype of cancer cell invasion controlled by fibril diameter and pore size of 3D collagen networks. *Biomaterials* **52**, 367–375 (2015).
35. J. Sapudom *et al*., Fibril bending stiffness of 3D collagen matrices instructs spreading and clustering of invasive and non-invasive breast cancer cells. *Biomaterials* **193**, 47–57 (2019).
36. E. M. Chandler *et al*., Implanted adipose progenitor cells as physicochemical regulators of breast cancer. *Proc. Natl. Acad. Sci. U.S.A.* **109**, 9786–9791 (2012).
37. F. Bertolini, J. Y. Petit, M. G. Kolonin, Stem cells from adipose tissue and breast cancer: Hype, risks and hope. *Br. J. Cancer* **112**, 419–423 (2015).
38. C. B. Raub, B. J. Tromberg, S. C. George, *Second-Harmonic Generation Imaging*, F. S. Pavone, P. J. Campagnola, Eds. (CRC Press, 2013), pp. 1–26.
39. K. Wolf *et al*., Physical limits of cell migration: Control by ECM space and nuclear deformation and tuning by proteolysis and traction force. *J. Cell Biol.* **201**, 1069–1084 (2013).
40. M. Achilli, D. Mantovani, Tailoring mechanical properties of collagen-based scaffolds for vascular tissue engineering: The effects of pH, temperature and ionic strength on gelation. *Polymers* **2**, 664–680 (2010).
41. S. S. Verbridge *et al*., Oxygen-controlled three-Dimensional cultures to analyze tumor angiogenesis. *Tissue Eng. Part A* **16**, 2133–2141 (2010).
42. K. Franke, J. Sapudom, L. Kalbitzer, U. Anderegg, T. Pompe, Topologically defined composites of collagen types I and V as in vitro cell culture scaffolds. *Acta Biomater.* **10**, 2693–2702 (2014).
43. M. Plodinec *et al*., The nanomechanical signature of breast cancer. *Nat. Nanotechnol.* **7**, 757–765 (2012).
44. A. J. Licup *et al*., Stress controls the mechanics of collagen networks. *Proc. Natl. Acad. Sci. U.S.A.* **112**, 9573–9578 (2015).
45. H. Wang, A. S. Abhilash, C. S. Chen, R. G. Wells, V. B. Shenoy, Long-range force transmission in fibrous matrices enabled by tension-driven alignment of fibers. *Biophys. J.* **107**, 2592–2603 (2014).
46. Y. S. Choi, L. G. Vincent, A. R. Lee, M. K. Dobke, A. J. Engler, Mechanical derivation of functional myotubes from adipose-derived stem cells. *Biomaterials* **33**, 2482–2491 (2012).
47. V. B. Shenoy, H. Wang, X. Wang, A chemo-mechanical free-energy-based approach to model durotaxis and extracellular stiffness-dependent contraction and polarization of cells. *Interface Focus* **6**, 20150067 (2016).
48. H. Ahmadzadeh *et al*., Modeling the two-way feedback between contractility and matrix realignment reveals a nonlinear mode of cancer cell invasion. *Proc. Natl. Acad. Sci. U.S.A.* **114**, E1617–E1626 (2016).
49. M. L. Smith *et al*., Force-induced unfolding of fibronectin in the extracellular matrix of living cells. *PLoS Biol.* **5**, e268 (2007).
50. K. Wang *et al*., Breast cancer cells alter the dynamics of stromal fibronectin-collagen interactions. *Matrix Biol.* **60–61**, 86–95 (2017).
51. A. M. D. Wan *et al*., Fibronectin conformation regulates the proangiogenic capability of tumor-associated adipogenic stromal cells. *Biochim. Biophys. Acta* **1830**, 4314–4320 (2013).
52. Antia, M., Baneyx, G., Kubow, K. E., Vogel, V. Fibronectin in aging extracellular matrix fibrils is progressively unfolded by cells and elicits an enhanced rigidity response. *Faraday Discuss* **139**, 229–249; discussion 309–325, 419–420 (2008).
53. P. Pakshir *et al*., Dynamic fibroblast contractions attract remote macrophages in fibrillar collagen matrix. *Nat. Commun.* **10**, 1850 (2019).
54. M. Chrzanowska-Wodnicka, K. Burridge, Rho-stimulated contractility drives the formation of stress fibers and focal adhesions. *J. Cell Biol.* **133**, 1403–1415 (1996).
55. K. Kimura *et al*., Regulation of myosin phosphatase by Rho and Rho-associated kinase (Rho-kinase). *Science* **273**, 245–248 (1996).
56. E. Amin *et al*., Rho-kinase: Regulation, (dys)function, and inhibition. *Biol. Chem.* **394**, 1399–1410 (2013).
57. N. P. Talele, J. Fradette, J. E. Davies, A. Kapus, B. Hinz, Expression of α-smooth muscle actin determines the fate of mesenchymal stromal cells. *Stem Cell Rep.* **4**, 1016–1030 (2015).
58. W. W. Kilarski, B. Samolov, L. Petersson, A. Kvanta, P. Gerwins, Biomechanical regulation of blood vessel growth during tissue vascularization. *Nat. Med.* **15**, 657–664 (2009).
59. Y. H. Song, S. H. Shon, M. Shan, A. D. Stroock, C. Fischbach, Adipose-derived stem cells increase angiogenesis through matrix metalloproteinase-dependent collagen remodeling. *Integr. Biol.* **8**, 205–215 (2016).
60. P. DelNero *et al*., 3D culture broadly regulates tumor cell hypoxia response and angiogenesis via pro-inflammatory pathways. *Biomaterials* **55**, 110–118 (2015).
61. W. D. Comper, A. Veis, The mechanism of nucleation for in vitro collagen fibril formation. *Biopolymers* **16**, 2113–2131 (1977).
62. D. A. Cisneros, C. Hung, C. M. Franz, D. J. Muller, Observing growth steps of collagen self-assembly by time-lapse high-resolution atomic force microscopy. *J. Struct. Biol.* **154**, 232–245 (2006).
63. L. Kalbitzer, T. Pompe, Fibril growth kinetics link buffer conditions and topology of 3D collagen I networks. *Acta Biomater.* **67**, 206–214 (2018).
64. S. E. Szczesny, D. M. Elliott, Interfibrillar shear stress is the loading mechanism of collagen fibrils in tendon. *Acta Biomater.* **10**, 2582–2590 (2014).
65. N. A. Kurniawan, L. H. Wong, R. Rajagopalan, Early stiffening and softening of collagen: Interplay of deformation mechanisms in biopolymer networks. *Biomacromolecules* **13**, 691–698 (2012).
66. J. Y. Lee *et al*., YAP-independent mechanotransduction drives breast cancer progression. *Nat. Commun.* **10**, 1848 (2019).
67. A. Das, R. S. Fischer, D. Pan, C. M. Waterman, YAP nuclear localization in the absence of cell-cell contact is mediated by a filamentous actin-dependent, myosin II- and phospho-YAP-independent pathway during extracellular matrix mechanosensing. *J. Biol. Chem.* **291**, 6096–6110 (2016).
68. B. Zhao *et al*., Inactivation of YAP oncoprotein by the Hippo pathway is involved in cell contact inhibition and tissue growth control. *Genes Dev.* **21**, 2747–2761 (2007).
69. A. Elosegui-Artola *et al*., Force triggers YAP nuclear entry by regulating transport across nuclear pores. *Cell* **171**, 1397–1410.e14 (2017).
70. M. G. McCoy, B. R. Seo, S. Choi, C. Fischbach, Collagen I hydrogel microstructure and composition conjointly regulate vascular network formation. *Acta Biomater.* **44**, 200–208 (2016).
71. S. Ishihara *et al*., Substrate stiffness regulates temporary NF-κB activation via actomyosin contractions. *Exp. Cell Res.* **319**, 2916–2927 (2013).
72. S. Vlahopoulos, I. Boldogh, A. Casola, A. R. Brasier, Nuclear factor-kappaB-dependent induction of interleukin-8 gene expression by tumor necrosis factor alpha: Evidence for an antioxidant sensitive activating pathway distinct from nuclear translocation. *Blood* **94**, 1878–1889 (1999).
73. D. Martin, R. Galisteo, J. S. Gutkind, CXCL8/IL8 stimulates vascular endothelial growth factor (VEGF) expression and the autocrine activation of VEGFR2 in endothelial cells by activating NFkappaB through the CBM (Carma3/Bcl10/Malt1) complex. *J. Biol. Chem.* **284**, 6038–6042 (2009).
74. E. S. Wijelath *et al*., Heparin-II domain of fibronectin is a vascular endothelial growth factor-binding domain: Enhancement of VEGF biological activity by a singular growth factor/matrix protein synergism. *Circ. Res.* **99**, 853–860 (2006).
75. D. Lachowski *et al*., Matrix stiffness modulates the activity of MMP-9 and TIMP-1 in hepatic stellate cells to perpetuate fibrosis. *Sci. Rep.* **9**, 7299 (2019).
76. M. Keating, A. Kurup, M. Alvarez-Elizondo, A. J. Levine, E. Botvinick, Spatial distributions of pericellular stiffness in natural extracellular matrices are dependent on cell-mediated proteolysis and contractility. *Acta Biomater.* **57**, 304–312 (2017).
77. S. Lee, S. M. Jilani, G. V. Nikolova, D. Carpizo, M. L. Iruela-Arispe, Processing of VEGF-A by matrix metalloproteinases regulates bioavailability and vascular patterning in tumors. *J. Cell Biol.* **169**, 681–691 (2005).
78. K. A. Bertrand *et al*., Mammographic density and risk of breast cancer by age and tumor characteristics. *Breast Cancer Res.* **15**, R104 (2013).
79. T. Li *et al*., The association of measured breast tissue characteristics with mammographic density and other risk factors for breast cancer. *Cancer Epidemiol. Biomarkers Prev.* **14**, 343–349 (2005).
80. J. M. Phillip, I. Aifuwa, J. Walston, D. Wirtz, The mechanobiology of aging. *Annu. Rev. Biomed. Eng.* **17**, 113–141 (2015).